Heliyon 10 (2024) e33651

Contents lists available at ScienceDirect

Heliyon

journal homepage: www.cell.com/heliyon

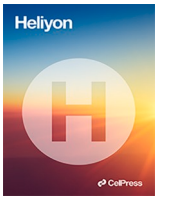

Research article

First-principles study of electronic, mechanical, and optical properties of M_3GaB_2 (M = Ti, Hf) MAX phases

A.K.M. Naim Ishtiaq [a], Md Nasir Uddin [a], Noor Afsary [a,*], Md Koushik Alam [a], Shariful Islam [a], Md Omar Faruk Rasel [a], Md Ashraf Ali [b,**], Karimul Hoque [a,***]

[a] Physics Discipline, Khulna University, Khulna, 9208, Bangladesh
[b] Department of Physics, Chittagong University of Engineering and Technology (CUET), Chattogram, 4349, Bangladesh

ARTICLE INFO

Keywords:
DFT study
MAX phases
Mechanical properties
Electronic properties
Optical properties

ABSTRACT

Integrating ceramic and metallic properties in MAX phases makes them highly desirable for diverse technological applications. In this study, through first-principles density functional theory (DFT), we investigated the physical properties of two new 312 MAX compounds, M_3GaB_2 (M = Ti, Hf). Chemical stability is confirmed via formation energy assessment, while mechanical stability is established by determining elastic stiffness constants. A thorough analysis of mechanical behaviors includes bulk modulus, shear modulus, Young's modulus, and hardness parameters. M_3GaB_2 demonstrates elastic constants and moduli closely aligned with other 312 carbides. Understanding the electronic band structure and density of states (DOS) sheds light on metallic properties, with anisotropy in electrical conductivity clarified through energy dispersion analysis. Investigation of photon interaction with titled compounds, including dielectric constants (real and imaginary parts), refractive index, absorption coefficient, photoconductivity, reflectivity, and energy loss function, has been carried out. The potential of M_3GaB_2 borides as a coating to reduce solar is evaluated based on the reflectivity spectra. These findings deepen our understanding of material properties and suggest diverse applications for M_3GaB_2 in various technological domains.

1. Introduction

Exploring novel compounds in the realm of advanced materials has long been a focal point of scientific inquiry and technological advancement. MAX phase materials have emerged as a significant area of interest in this field due to their unique blend of metallic and ceramic properties, offering diverse applications [1]. MAX phases, represented by the chemical formula $M_{n+1}AX_n$ (or MAX), are layered nanolaminate ternary carbides and nitrides that constitute a distinctive material class exhibiting both ceramic and metallic characteristics, where n can vary from 1 to 3 [1–3]. These phases feature early transition metals (e.g., Sc, Ti, Zr, Hf, V, Nb, Ta, Cr, Mn, and Mo) from groups 3–6, A representing a group of elements following the old American nomenclature (e.g., Al, Si, Ge, Sn, Pb, P, As, and S), and X being carbon, nitrogen, or boron [2–5]. With over 524 members, the MAX phases represent a family of inherently nano-laminated ternary compounds encompassing carbides, nitrides, and borides [6]. The M-X bonds in MAX phase materials are

* Corresponding author.
** Corresponding author.
*** Corresponding author.
E-mail addresses: noorafsary@gmail.com (N. Afsary), ashrafphy31@cuet.ac.bd (M.A. Ali), hoquekarimul@phy.ku.ac.bd (K. Hoque).

https://doi.org/10.1016/j.heliyon.2024.e33651
Received 1 March 2024; Received in revised form 11 June 2024; Accepted 25 June 2024
Available online 26 June 2024

exceptionally robust due to a combination of metallic and covalent bonding. In contrast, the M-A bonds exhibit comparatively lower strength, contributing to their layered structure. This characteristic imparts nanolaminate MAX materials with outstanding thermal and electrical conductivity, superior mechanical properties, and resilience against chemical degradation [7]. Among the diverse MAX phases, the 312 MAX phases are particularly intriguing. The high metallicity of MAX phases is attributed to a significant density of states (DOS) at the Fermi level, primarily contributed by the d-d orbitals of the M-element [8]. Similar to the 211 phases, the metallic character of the 312 phases is predominantly governed by the contribution of M-d orbitals. Notably, the 312 phase possesses the possibility of being etched out the A-layers, forming new 2D materials known as MXenes [9].

The MAX phase family initially expanded to $M_{n+1}AX_n$, with n variably equaling 1 or 2, following the initial discoveries of Ti_3SiC_2 and Ti_3GeC_2 [10,11]. Since then, a plethora of M_3AX_2 phases have been developed. In 1994, Pietzka et al. conducted a comprehensive investigation on Ti_3AlC_2 using wet chemistry methods [12]. Lin et al. achieved direct atomic resolution of layered ternary Ta–Al–C carbides, focusing on the stacking properties of TaC_x slabs and aluminum (Al) atomic planes and reported the bulk modulus [13]. In 2016, Lapauw et al. reported the synthesis and structural characterization of Zr_3AlC_2 and Hf_3AlC_2, marking the introduction of the first members of the 312 MAX phases in the Hf-Al-C system [14,15]. Subsequently, in 2017, Lapauw synthesized Ti_3SnC_2, Zr_3SnC_2, and Hf_3SnC_2 MAX phases and characterized them using X-ray diffraction [16]. The synthesis of Ti_3ZnC_2, employing a replacement reaction between late transition-metal halides and MAX phase precursors, was presented by Li et al. in 2019, representing a unique top-down synthesis approach for nano-laminated materials [17]. In 2023, Zhang et al. reported the synthesis of two new 312 MAX phases, Zr_3PbC_2 and Hf_3PbC_2, through spark plasma sintering, marking the first discovery of lead-containing 312 MAX phases [18].

The synthesis of MAX phase borides has expanded the MAX family, with theoretical investigations conducted by Khazaei et al. and Surucu et al. [19,20]. Khazaei et al. pioneered the prediction of stability for M_2AlB (M = Sc, Ti, Cr, Zr, Nb, Mo, Hf, and Ta) compounds through the calculation of formation energies while also exploring their electronic and mechanical properties [19]. Surucu et al. conducted a comprehensive study on the structural, electrical, elastic, and lattice dynamical characteristics of M_2AB (M = Ti, Zr, Hf; A = Al, Ga, In) compounds, noting the ductility of Ti_2AB and Hf_2AB [20]. Additionally, Miao et al. predicted several B-based thermodynamically stable MAX phases and Mxenes [21]. Ali et al. utilized first-principles calculations to investigate further the M_2SB (M = Zr, Hf, and Nb) MAX compounds [22], previously synthesized by Rackl et al. [23]. In recent years, significant attention has been devoted to studying the electronic-structural, thermo-electric, and thermo-mechanical properties of M_2AC and M_2AB (M = Nb or Mo, A = Al or Ga) compounds, revealing Ga as a promising A element for boride phases [24–26]. Despite extensive research on 211 MAX phases, no report on the 312 MAX phase borides is available to date. Thus, for our present study, we have selected Ti_3GaB_2 and Hf_3GaB_2 in the first attempt of 312 MAX phase borides, which is the main significance of this study.

In this study, we employ first-principles density functional theory (DFT) to investigate the ground state physical properties of Ti_3GaB_2 and Hf_3GaB_2. This investigation aims to shed light on how their elemental composition intricately influences their properties by comparing the obtained results with those of their carbide counterparts. Our analysis encompasses their chemical and mechanical stability, electronic band structure, and optical response to incident photons. Ti_3GaB_2 and Hf_3GaB_2 showcase remarkable properties, blending ceramic and metallic characteristics, thus making them highly attractive for diverse technological applications. Furthermore, the assessment of their potential as a coating material for mitigating solar heating underscores the practical significance of our investigation. Overall, this research aims to contribute to the advancement of materials science and pave the way for the development of innovative technologies, harnessing the considerable potential of MAX phase materials across various industries.

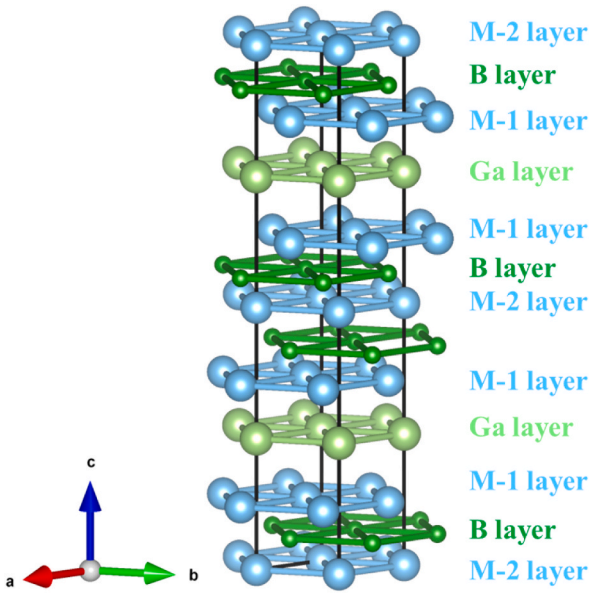

Fig. 1. The schematic unit cell structure of M_3GaB_2.

2. Computational methodology

We utilized the Cambridge Serial Total Energy Package (CASTEP) module within Materials Studio 2020 to conduct first-principles DFT computations [27,28]. The electronic exchange and correlation were treated using the generalized gradient approximation (GGA) of Perdew-Burke-Ernzerhof [29]. Vanderbilt-type ultrasoft pseudopotentials were employed to describe the electrostatic interaction between valence electrons and ionic cores. We perform Pseudo-atomic calculations for the electronic orbitals of Ti (Ti - $3s^2\ 3p^6\ 3d^2\ 4s^2$), Hf (Hf - $5d^2\ 6s^2$), Ga (Ga - $3d^{10}\ 4s^2\ 4p^1$), and B (B - $2s^2\ 2p^1$). For plane wave expansion, we select a cutoff energy of 400 eV. Then, we utilized the Monkhorst-Pack approach to generate a 13 × 13 × 2 k-point mesh for integration across the first Brillouin zone [30]. We employed the density mixing approach to optimize the electronic structure, with atomic positions determined using the Broyden et al. algorithm [31]. Comprehensive testing of Brillouin zone sampling and kinetic energy cutoff ensured convergence. Convergence thresholds were set as follows: 5.0×10^{-7} eV/atom for energy, 5.0×10^{-6} eV/atom for self-consistent field tolerance, 0.01 eV/Å for maximum force, 5.0×10^{-4} Å for maximum displacement, and 0.02 GPa for maximum stress. The Broyden-Fletcher-Goldfarb-Shanno (BFGS) minimization method [31]was employed to systematically determine electronic wave functions and resultant charge density to elucidate the ground state structural characteristics of the studied phases. The total energies of the unit cell were computed utilizing periodic boundary conditions. The intrinsic "stress-strain" technique within the CASTEP program was utilized to derive elastic constants, which were subsequently used to calculate elastic moduli based on the estimated elastic constant tensors C_{ij}.

3. Results and discussion

3.1. Structural properties

Fig. 1 depicts the unit cell structure of M_3GaB_2 (M = Ti, Hf) 312 MAX phases. Like other MAX phases, M_3GaB_2 (M=Ti, Hf), featuring a hexagonal structure, belongs to the P63/mmc space group. Each unit cell comprises 12 atoms, with two formula units contained within. In the optimized structure presented in Fig. 1, the Wyckoff positions 2a and 4f are occupied by M atoms, with respective fractional coordinates of (0, 0, 0) and (2/3, 1/3, 0.1383). Ga atoms reside at the 2b Wyckoff site, with fractional coordinates of (0, 0, 1/4), while B atoms are positioned in the 4f Wyckoff positions, with fractional coordinates of (1/3, 2/3, 0.0719).

Table 1 presents the geometry-optimized unit cell parameters alongside corresponding experimental and theoretical values. Our computed values exhibit satisfactory agreement with both theoretically anticipated and experimentally determined values reported prior to the compound's synthesis.

As we aim to characterize the MAX phase borides for the first time, it is imperative to calculate the formation energy to validate their stability. The formation energy of M_3GaB_2 (M = Ti, Hf) was determined using the established formula commonly employed for predicting MAX phase materials by Eq. (1) [34].

$$E_{for}^{M_3GaB_2} = \frac{E_{total}^{M_3AB_2} - \left(xE_{solid}^{M} + yE_{solid}^{Ga} + zE_{solid}^{B}\right)}{x+y+z}\ ;\ \mathrm{M = Ti, Hf.} \tag{1}$$

In this context, the notation x = 6, y = 2, and z = 4 represents the quantities of M, Ga, and B atoms within the unit cell. The total energies of the M_3GaB_2 MAX phase and the stable structures of individual atoms (M, Ga, and B) are represented by the symbols $E_{total}^{M_3AB_2}$, E_{solid}^{M}, E_{solid}^{Ga}, and E_{solid}^{B}, respectively. The predicted formation energies for Ti_3GaB_2 and Hf_3GaB_2 are −1.408 eV/atom and −1.458 eV/atom, respectively.

3.2. Electronic properties

3.2.1. Band structure

A comprehensive understanding of the optical and transport properties of solids necessitates a thorough grasp of the electronic band structure (EBS). Fig. 2 presents the energy-dependent EBS of M_3GaB_2 (M = Ti, Hf) calculated along high-symmetry points in k-space. The Fermi level (E_F), representing states at T = 0 K, is indicated by a horizontal dashed line. The metallic nature of the EBS is readily apparent and characterized by a significant overlap between valence and conduction bands. Several valence bands intersect the E_F along the *K–G* and *G–M* directions, depicted in black, overlapping with conduction bands, resulting in a non-zero total DOS at E_F. Furthermore, the EBS reveals direction-specific electrical conductivity, as evidenced by differences in energy dispersion. Paths along the c-direction (*G-A*, *H–K*, and *M-L*) exhibit reduced energy dispersion compared to those in the basal planes (*A-H*, *K-G*, *G-M*, and *L-H*) [35].

Table 1
Calculated lattice constants (*a* and *c*), *c*/*a* ratio, Z_M, Z_B, and volume (*V*) of M_3GaB_2 (M = Ti, Hf).

Phase	*a* (Å)	*c* (Å)	*c*/*a*	Z_M	Z_B	*V* (Å^3)
Ti_3GaB_2	3.15	19.20	6.09	0.133	0.070	165.11
Hf_3GaB_2	3.38	20.04	5.92	0.138	0.071	199.03
[32] Ti_3GaC_2	3.08	18.24	5.92	0.129	0.069(Z_c)	
[33] Hf_3AlC_2	3.28	19.66	5.99	0.132	0.0712(Z_c)	183.66

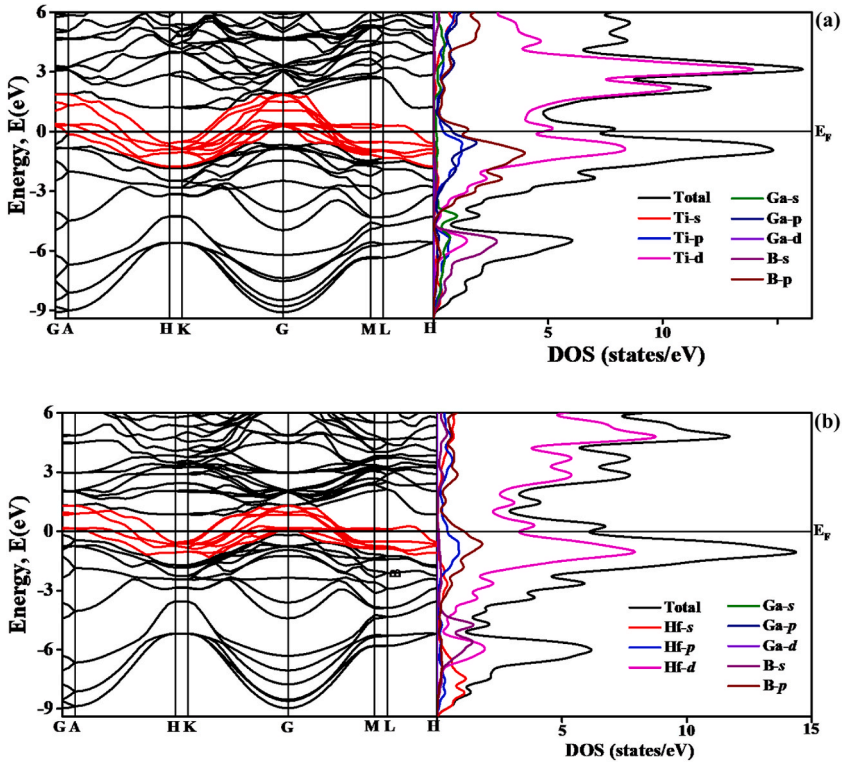

Fig. 2. Ebs and DOS of (a) Ti_3GaB_2 and (b) Hf_3GaB_2.

The observed disparity in energy dispersion suggests a direction-dependent electrical conductivity, indicating a reduced level of energy dispersion along the c-axis compared to the ab-plane. Consequently, indicating a higher electronic effective mass tensor for conduction along the c-axis, relative to the ab-basal plane, implies an anticipated decrease in electrical conductivity along the c-direction [36]. This characteristic arises from the densely packed layers of M and A atoms, along with the interstitial X atoms, contributing to the material's layered configuration and resulting in anisotropic properties, wherein the material exhibits varying traits along distinct crystallographic axes [19]. The bonding nature within MAX phases profoundly influences their electronic band structure. Covalent bonds between Ti/Hf and B atoms lead to partially filled electron bands, thereby contributing to metallic conductivity. In contrast, ionic bonding between Ga and B atoms may induce localized electron states, which can impact the EBS near the Fermi level. These bonding characteristics give rise to intriguing electronic properties in MAX phases, including enhanced thermal stability, excellent electrical conductivity, and robust mechanical properties [37].

3.2.2. Density of state (DOS)

We conducted computations on the total and partial DOS for M_3GaB_2 (M = Ti, Hf) borides to analyze bonding characteristics and the involvement of diverse electronic states in determining electronic conductivity. Fig. 2 illustrates the calculated DOS (total and partial) of the M_3GaB_2 phases, with the E_F denoted by a vertical dashed line. These figures reveal that the DOS maintains a significant magnitude at the Fermi energy, indicating metallic properties for all compounds [20]. To understand atomic orbitals bond, DOS can be divided into two categories: bonding, non-bonding states (<EF), and anti-bonding states (>EF) [19,38]. In Fig. 2, the bonding states involving the *d*-orbitals of M (M = Ti, Hf) and the *p*-orbitals of B are found at lower energy levels, resulting in the formation of strong covalent M − B bonds. Conversely, anti-bonding states between the *d*-orbitals of M and the *p*-orbitals of B are found at higher energy levels beyond the Fermi level. The bonding states of Ti_3GaB_2 and Hf_3GaB_2 compounds, shown in Fig. 2, are partially filled with electrons due to the pseudo-gap shifting to the right relative to the Fermi level [19]. Additionally, Fig. 2 shows that the Ti(*s*), Ga(*d*), B(*s*) orbitals in the Ti_3GaB_2 compound and the Ga (*s*, *p*, *d*), B(*s*) orbitals in the Hf_3GaB_2 compound do not contribute to bond formation below the Fermi level, indicating that these electronic states are non-bonding states. Consequently, there is a rapid increase in states at the Fermi energy level, leading to an elevation of the Fermi energy level to a higher energy level range. At the Fermi level, Ti-d and Hf-d orbitals are mainly responsible for the electronic contribution in the V.B and C.B. The DOS, N(E_F), at the E_F for Ti_3GaB_2 and Hf_3GaB_2, as depicted in Fig. 2, is 7.52 and 6.13 electronic states per unit cell per eV, respectively. This discrepancy in N(EF) among the M_3GaB_2 compounds suggests significant variations in electronic transport properties within this group [39]. The partial DOS serves as a valuable tool for uncovering hybridization among distinct states. The energy range of the valence band can be segmented into two intervals: −9.1 eV to −4.7 eV and −4.7 eV to −0.0 eV. In the case of Ti_3GaB_2 and Hf_3GaB_2, strong hybridization is observed between M-d and B-s, resulting in prominent peaks in the low-energy region of the total DOS. Additionally, in the energy range from 0 eV to −6

eV, M-d dominates, displaying hybridization with Ga-p and B-p for both Ti_3GaB_2 and Hf_3GaB_2 compounds.

The Fermi surface (FS), depicted in reciprocal space, delineates between occupied and unoccupied electron states at zero temperature. The behavior of an electron on the FS is dictated by its position, and the arrangement of the FS relative to the Brillouin zone offers valuable insights into understanding the electrical, magnetic, and thermal properties of metals or metallic compounds. As illustrated in Fig. 3, the FS of both Ti_3GaB_2 and Hf_3GaB_2 consists of seven sheets. In a previous discussion regarding electronic configuration, we found that both compounds exhibit nearly identical DOS profiles.

This similarity is attributed to their nearly equal number of Fermi sheets. Several shared characteristics are apparent across all FSs, including electron-like sheets centered along the G–A direction. These layers exhibit entirely cylindrical and/or prismatic formations characterized by hexagonal cross-sections. Additionally, hole-like sheets with complex topologies were observed along the H–K direction, positioned at the corners of the Brillouin zone.

3.3. Mechanical Properties

Elastic characteristics garner significant interest due to their ability to assess various fundamental macroscopic attributes of materials. The MAX phases, characterized by hexagonal crystalline structures, possess five distinct elastic tensors—C_{11}, C_{12}, C_{13}, C_{33}, and C_{44}. These coefficients are established through the 'stress-strain' methodology, as implemented in the CASTEP software [40]. The elastic properties of polycrystals are determined by employing Voigt-Reuss-Hill approximations, which are derived from the elastic constants of single crystals [41–43]. The computed elastic parameters, as well as those from alternative computations [44,45], are presented in Table 2. For MAX compounds to exhibit dynamic stability, specific conditions must be satisfied [44–46]: C_{11} must be greater than 0, $C_{11} - C_{12}$ must be greater than 0, C_{44} must be greater than 0, and $(C_{11} + C_{12})\, C_{33} - 2C_{13}{}^{*}C_{13}$ must be greater than 0. The listed elastic constants (C_{ij}) meet the specified criteria for the M_3GaB_2 (M = Ti, Hf) compound, indicating their mechanical stability. Additionally, they offer insights into the mechanical properties of the M_3GaB_2 (M = Ti, Hf) MAX phases under investigation. In the Ti_3GaB_2 compound, C_{11} is less than C_{33}, whereas, in the Hf_3GaB_2 compound, C_{11} is greater than C_{33}, suggesting that Hf_3GaB_2 is more resistant to compression along the *a*-axis compared to the *c*-axis. This observation implies elastic anisotropy in the studied Hf_3GaB_2 compounds. Referring to Fig. 1, the varying atomic configurations along various crystallographic axes lead to variations in bonding strengths, as reflected by the unequal values of C_{11} and C_{33}. In hexagonal systems, C_{11} measures resistance to deformation along the *a (b)*-axis, while C_{33} indicates the same along the c-axis. The higher C_{11} than C_{33} in Hf_3GaB_2 borides signifies greater bonding strength, stiffness, and resistance to deformation along the a(*b*)-axis compared to the c-axis, contributing to their elastic anisotropy. Conversely, the smaller C_{11} compared to C_{33} in Ti_3GaB_2 suggests relatively lower bonding strength, stiffness, and resistance than Hf_3GaB_2. Table 2 shows that the Ti and Hf-containing 312 MAX phase carbides exhibit greater stability than MAX phase borides.

As illustrated in Table 2, the stiffness constants of the 312 carbides surpass those of the 312 borides in our study. For example, the C_{11} values for Ti_3GaB_2 are 54% and 55% lower than those for Ti_3GaC_2 and Ti_3SiC_2, respectively, while Hf3GaB2 shows reductions of 33% and 28% compared to Hf_3AlC_2 and Hf_3SnC_2, respectively. Similar patterns are observed for C_{33}, C_{44}, and C_{13}. Specifically, Ti_3GaB_2 exhibits C_{33} values that are 25% and 38% lower, and C_{44} values that are 26% and 42% lower, than those for Ti_3GaC_2 and Ti_3SiC_2, respectively. For Hf_3GaB_2, C_{33} values are 30% and 32% lower, and C_{44} values are 25% and 17% lower, than those for Hf_3AlC_2 and Hf_3SnC_2, respectively. However, in the case of C_{12}, Ti_3GaB_2 values are 37% and 20% higher than those for Ti_3GaC_2 and Ti_3SiC_2, respectively. For Hf_3GaB_2, the C_{12} values are 9% higher and 12% lower than those for Hf_3AlC_2 and Hf3SnC$_2$, respectively.

The elastic moduli—bulk modulus (*B*), shear modulus (*G*), and Young's modulus (*Y*)—characterize the mechanical responses of materials in polycrystalline forms. Table 2 also presents the bulk modulus (*B*) and shear modulus (*G*), calculated using Hill's approximation [43]. These values represent averages between the upper limit (Voigt [41]) and lower limit (Reuss [42]) of *B* as per Hill's method. The detailed calculations are illustrated by Eq. (2) and Eq. (3) as follows [48]:

$$\left.\begin{aligned} B = (B_V + B_R)/2 \text{ here}, B_V = [2(C_{11} + C_{12}) + C_{33} + 4C_{13}]/9 \text{ and } B_R = C^2/M, \text{also} \\ C^2 = (C_{11} + C_{12})C_{33} - 2C_{13}^2 \text{ and } M = C_{11} + C_{12} + 2C_{33} - 4C_{13} \end{aligned}\right\} \quad (2)$$

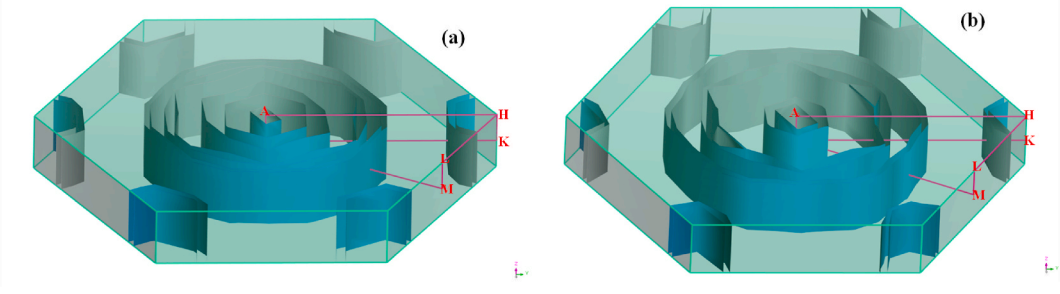

Fig. 3. FS topology of (a) Ti_3GaB_2 and (b) Hf_3GaB_2.

Table 2
The stiffness constants, elastic moduli, Pugh's ratio (G/B), and hardness parameters M_3GaB_2 (M = Ti, Hf).

Parameters	Ti_3GaB_2	Hf_3GaB_2	[32] Ti_3GaC_2	[47] **Ti_3SiC_2**	[33] Hf_3AlC_2	[44] **Hf_3SnC_2**
C_{11} (GPa)	166	231	359	365	347	320
C_{33} (GPa)	219	203	292	352	291	300
C_{44} (GPa)	91	95	123	156	127	115
C_{12} (GPa)	107	84	78	89	77	95
C_{13} (GPa)	68	87	69	99	80	96
B (GPa)	115	131	159	184	162	168
G (GPa)	56	79	130	143	127	112
Y (GPa)	144	197	306	341	302	275
ν	0.29	0.25	0.1787	0.19	0.19	0.22
B/G	2.06	1.66	1.2231	1.28	1.28	1.50
G/B	0.48	0.60	0.81	0.78	0.78	0.67
H_{macro} (GPa)	6.00	11.1	24.2	24.1	22.5	16.6
H_{micro} (GPa)	7.8	13.2	27.6	29.6	26.2	21.1

$$\left.\begin{aligned} G = (G_V + G_R)/2 \text{ where, } G_V = (M + 12C_{44} + 12C_{66})/30 \text{ and} \\ G_R = \left(\frac{5}{2}\right)\left[C^2C_{44}C_{66}\right]/\left[3B_VC_{44}C_{66} + C^2(C_{44} + C_{66})\right] \end{aligned}\right\} \quad (3)$$

The computed bulk modulus and shear modulus values for M_3GaB_2 (M = Ti, Hf) MAX phase borides are smaller than those for MAX phase carbides (Ti_3GaC_2 and Hf_3AlC_2). Consequently, it can be inferred that MAX phase carbides exhibit higher resistance to volume and plastic deformations than borides of the same structure. A high value of G indicates hardness, whereas a low value suggests softness. Accordingly, Hf_3GaB_2 is harder than Ti_3GaB_2. Young's modulus (Y) is another crucial mechanical property that measures a material's tensile stiffness which is calculated by, $= 9BG/(3B+G)$. Ti_3GaB_2 exhibits the lower Y value compared to Hf_3GaB_2, indicating that Hf_3GaB_2 is stiffer than Ti_3GaB_2. Notably, 312 MAX phase carbides are generally stiffer than their boride counterparts.

The mechanical properties of boride phases are typically inferior to those of carbide phases. This discrepancy is clearly illustrated through specific comparisons. For instance, the bulk modulus (B), shear modulus (G), and Young's modulus (Y) of Ti_3GaB_2 are substantially lower than those of their carbide counterparts. Ti_3GaB_2 has B, G, and Y values that are 27%, 56%, and 52% lower, respectively, than those of Ti_3GaC_2 carbides. When compared to Ti_3SiC_2 carbides, these values for Ti_3GaB_2 are 37%, 61%, and 58% lower. Similarly, Hf_3GaB_2 exhibits the same trend. Its bulk modulus, shear modulus, and Young's modulus are 19%, 37%, and 34% lower, respectively, than those of Hf_3AlC_2 carbides. In comparison to Hf_3SnC_2 carbides, the values for Hf_3GaB_2 are 22%, 29%, and 28% lower.

Pugh's ratio, the ratio of bulk modulus (B) to shear modulus (G), defined by B/G serves as a predictor for the ductile or brittle nature of a material [49]. A Pugh's ratio exceeding 1.75 suggests ductility, while a value below 1.75 indicates brittleness. The Pugh's ratio values for Ti_3GaB_2 and Hf_3GaB_2 are 2.06 and 1.67, respectively. Thus, Ti_3GaB_2 is classified as ductile, whereas Hf_3GaB_2 is considered brittle. Poisson's ratio (ν), another crucial elastic parameter in polycrystalline materials defined by, $\upsilon = (3B - Y)/(6B)$ offers insights into their mechanical behaviors, akin to Pugh's ratio. A ν value less than 0.26 characterizes brittle materials, while a higher value indicates ductile behavior [50]. In the case of Ti_3GaB_2, Poisson's ratio predicts ductility, whereas for Hf_3GaB_2, it suggests brittleness. Though MAX phases are usually brittle, some ductile phases were reported previously which are Nb_2SC and Sc_2GaB [22,25]. Poisson's ratio also aids in identifying inter-atomic forces in solids [51]. If ν falls within the range of 0.25–0.50, it indicates effective central forces. Outside this range, non-central interatomic forces dominate. Consequently, the M_3GaB_2 (M = Ti, Hf) MAX phases are governed by non-central interactions. Brittleness often correlates with non-central forces, which exhibit pronounced angular characteristics [51].

Hardness is a critical parameter for designing various devices in engineering applications. The elastic moduli of polycrystalline materials provide insights into hardness values, where resistance to indentation correlates with material hardness. We have determined both micro-hardness (H_{micro}) and macro-hardness (H_{macro}). H_{micro} is influenced by Young's modulus and Poisson's ratio, while H_{macro}, also known as Chen's hardness, is determined by Eq. (4) using shear and bulk moduli [52,53].

$$H_{macro} = 2\left[\left(\frac{G}{B}\right)^2 G\right]^{0.585} - 3, \text{ and } H_{micro} = \frac{(1-2\upsilon)Y}{6(1+\upsilon)} \quad (4)$$

Table 2 shows the computed values of H_{micro} and H_{macro}. These values reveal that Hf_3GaB_2 exhibits greater hardness than Ti_3GaB_2, consistent with elastic constants and moduli. In contrast, the 312 borides demonstrate significantly lower hardness compared to the 312 carbides. Specifically, the H_{macro} values for Ti_3GaB_2 are 75% lower than those for Ti_3GaC_2 and Ti_3SiC_2, while Hf_3GaB_2 shows decreases of 51% and 33% relative to Hf_3AlC_2 and Hf_3SnC_2, respectively. Similarly, in terms of H_{micro}, the hardness values for Ti_3GaB_2 are reduced by 72% and 74% compared to Ti_3GaC_2 and Ti_3SiC_2, respectively. For Hf_3GaB_2, the H_{micro} values are 50% and 37% lower than those for Hf_3AlC_2 and Hf_3SnC_2, respectively.

3.4. Vickers hardness

Hardness, as a characteristic of a solid material, signifies its resistance to plastic deformation, indentation, penetration, and scratching. Experimental hardness values vary depending on testing methods temperature, and other variables. In a similar vein, the formalism used in the computations has an impact on the theoretical values. In a similar vein, the formalism used in the computations has an impact on the theoretical values. A formula initially proposed by Gao [54] for non-metallic covalent materials was modified by Gou et al. [55] to allow for partially metallic compounds such as the ternaries being studied. The bond hardness can be calculated using Eq. (5) as follows:

$$H_v^{\mu} = 740(P^{\mu} - P^{\mu'})\left(v_b^{\mu}\right)^{(-5/3)} \tag{5}$$

In this context, P^{μ} refers to the Mulliken overlap population of the m-type bond, $P^{\mu'}$ denotes the metallic population, which is determined using the volume of the unit cell V and the number of free electrons in a cell given by $n_{free} = \int_{E_p}^{E_f} N(E)dE$, where E_f and E_p represent the Fermi and pseudogap energies, respectively. Then, $P^{\mu'} = n_{free}/V$, v_b^{μ} denotes the volume of an μ-type bond, it can be calculated using the bond length d^{μ} of type μ and the number of bonds N_b^{μ} of type v per unit volume, represented by the equation $v_b^{\mu} = (d^{\mu})^3 / \sum_{\upsilon}\left[(d^{\mu})^3 N_b^{\mu}\right]$. The hardness of a crystal with a complicated multiband structure can be calculated using the geometric mean of all bond hardnesses, as expressed by Eq. (6) as follows [56,57]:

$$H_V = \left[\Pi^{\mu}\left(H_v^{\mu}\right)^{n^{\mu}}\right]^{1/\sum n^{\mu}} \tag{6}$$

Table 3 displays the hardness values of the investigated borides and the hardness of each bond. These results consider only the plausible and positive populations between nearby atoms.

Vickers hardness values for the Ti_3GaB_2 and Hf_3GaB_2 compounds are 4.7 Gpa and 4.88 Gpa, respectively. The comparison reveals that the Hf-based boride is harder than the Ti-based boride. However, both compounds exhibit relatively low hardness values, falling within the range of 2–8 GPa [58]. This implies their soft nature and favorable machinability. The Vickers hardness (Hv) value of the previously synthesized carbide, Hf_3AlC_2, Ti_3SnC_2 and Hf_3SnC_2 [33,44], is also included in Table 3. The hardness values of the named compounds are found to be perfectly aligned with M_3GaB_2 (M = Ti and Ga). Variations in bonding strength, valence electron concentration, and other factors probably cause this discrepancy. The Vickers hardness of 312 borides is consistent with that of their carbide counterparts. For instance, when comparing the hardness of Ti_3GaB_2 to Hf_3AlC_2, Ti_3SnC_2, and Hf_3SnC_2, we observed that it is 4% and 8% lower, respectively, but equal to the hardness of Hf_3SnC_2. For Hf_3GaB_2, the hardness is 2% greater than Hf_3SnC_2, but 2% and 6% lower than Hf_3AlC_2 and Ti_3SnC_2, respectively.

3.5. Optical properties

When subjected to electromagnetic radiation, materials display diverse behaviors, manifesting in two primary physical phenomena: energy conversion (absorption, reflection, and inelastic scattering) and propagation. This section aims to discuss the interaction incident photon with M_3GaB_2 (M = Ti, Hf) compounds, with the intention of exploring their suitability for practical applications. The optical characteristics for polarization vectors ([100]) of the M_3GaB_2 (M = Ti, Hf) compounds are computed and illustrated in Fig. 5 for incident photon energies up to 25 eV. Considering the metallic properties exhibited by the investigated MAX phase compounds according to the band structure, all computations have been conducted utilizing the Drude term. This term encompasses a plasma frequency of 3 eV, damping of 0.05 eV, and Gaussian smearing of 0.5 eV [59]. The optical constants play a pivotal role in influencing the material's response to incident radiation. One of the primary optical features of solids is the complex dielectric functions, denoted as $\varepsilon(\omega) = \varepsilon_1(\omega) + i\varepsilon_2(\omega)$. The imaginary part of the dielectric constant denotes the absorption of light energy, representing the amount of light absorbed as it traverses the material. A higher imaginary dielectric constant indicates increased absorption of light at particular

Table 3
Calculated data for Mulliken bond number (n^{μ}), bond length (d^{μ}), bond overlap populations (P^{μ}), metallic populations ($P^{\mu'}$), Vickers hardness (H_V) M_3GaB_2 (M = Ti, Hf) compounds.

Compounds	Bond	n^{μ}	d^{μ}(Å)	P^{μ}	$P^{\mu'}$	V_b^{μ}	H_v (GPa)
Ti_3GaB_2	B1–Ti1	4	2.188	1.31	0.064	19.52	4.7
	B2–Ti2	4	2.268	0.84	0.064	21.74	
Hf_3GaB_2	B1-Hf1	4	2.364	1.75	0.057	23.86	4.88
	B2-Hf2	4	2.429	1.21	0.057	25.89	
[33] Hf_3AlC_2	Hf–C	4	2.271	1.46	0.071	10.61	4.9
	Hf–C	4	2.381	1.02	0.071	15.62	
	Hf–Al	4	3.00	0.78	0.071	47.32	
[44] Ti_3SnC_2	Ti1-C	4	2.095	1.21	0.012	18.28	5.1
	Ti2-C	4	2.220	0.87	0.012	21.77	
[44] Hf_3SnC_2	Hf1-C	4	2.281	1.57	0.016	22.74	4.7
	Hf2-C	4	2.388	1.07	0.016	25.87	

wavelengths.

On the other hand, the real part of the dielectric constant characterizes the polarization of the material. It describes the speed of light, with a higher value indicating slower light propagation. The imaginary part of the dielectric function, $\varepsilon_2(\omega)$, can be calculated using Eq. (7) as follows [60]:

$$\varepsilon_2(\omega) = \frac{2e^2\pi}{\Omega\varepsilon_0}\sum_{k,v,c}\left|\psi_k^c\left|u.r\right|\psi_k^v\right|^2\delta\left(E_k^c - E_k^v - E\right) \tag{7}$$

In this case, ω denotes the light's angular frequency, e is the electronic charge, u is the vector defining the incident electric field's polarization, and the conduction and valence band wave functions at point K are, respectively, represented by ψ_k^c and ψ_k^v. The real part $\varepsilon_1(\omega)$ of the dielectric function can be obtained from the imaginary part $\varepsilon_2(\omega)$ using the Kramers-Kronig relations, as expressed by Eq. (8) [61]:

$$\varepsilon_1(\omega) = 1 + \frac{2}{\pi}P\int_0^\infty \frac{\omega'\varepsilon_2(\omega')d\omega'}{(\omega'^2 - \omega^2)} \tag{8}$$

The real component of the complex dielectric function for M_3GaB_2 (M = Ti, Hf) is depicted in Fig. 4(a), while Fig. 4(b) illustrates its imaginary component. This illustration is essential to understanding how the material responds to incident photons. The negative value observed in the real part and the positive value in the high imaginary part of the dielectric function correspond consistently with the band structure analysis. The real part approaches zero at approximately 1.066 eV for both compounds and subsequently becomes negative. The imaginary part becomes zero at around 18.44 eV. This observation corroborates the metallic properties of the material.

The reflectivity and loss function can be computed from the dielectric function using the following Eq. (9) [62,63,]:

$$R(\omega) = \left|\frac{\sqrt{\varepsilon(\omega)} - 1}{\sqrt{\varepsilon(\omega)} + 1}\right|^2 \text{ and } L(\omega) = \varepsilon_2(\omega) \Big/ \left[\{\varepsilon_1(\omega)\}^2 + \{\varepsilon_2(\omega)\}^2\right] \tag{9}$$

Fig. 4 (c) illustrates the reflectivity curve, where the reflectivity begins at 0.75 for Ti_3GaB_2 and 0.76 for Hf_3GaB_2. Subsequently, both curves gradually decrease, followed by the emergence of distinct peaks. MAX phases are deemed suitable for coating materials when their reflectivity exceeds 44 % [59]. The data indicates that the reflectivity for Ti_3GaB_2 consistently stays above 44% in both the infrared and visible regions. However, for Hf_3GaB_2, it exceeds this threshold in the infrared (IR) region but decreases in the visible region. As a result, Ti_3GaB_2 seems to be a promising option for coating applications. Our investigation demonstrates significant consistency with the results observed for Zr_3PbC_2. Specifically, we found that the R(0) value lies between 0.6-0.7 eV. Following this, there is a continuous decrease in the reflectivity spectrum, mirroring the trend observed in our study.

Fig. 4(d) illustrates the loss function. The loss function, reflection, and absorption characteristics of a substance are interconnected. The electron energy-loss function is a crucial optical characteristic that describes the energy loss that an electron experiences when it moves quickly through a medium. The highest peak in the loss spectrum signifies the plasma resonance induced by collective charge

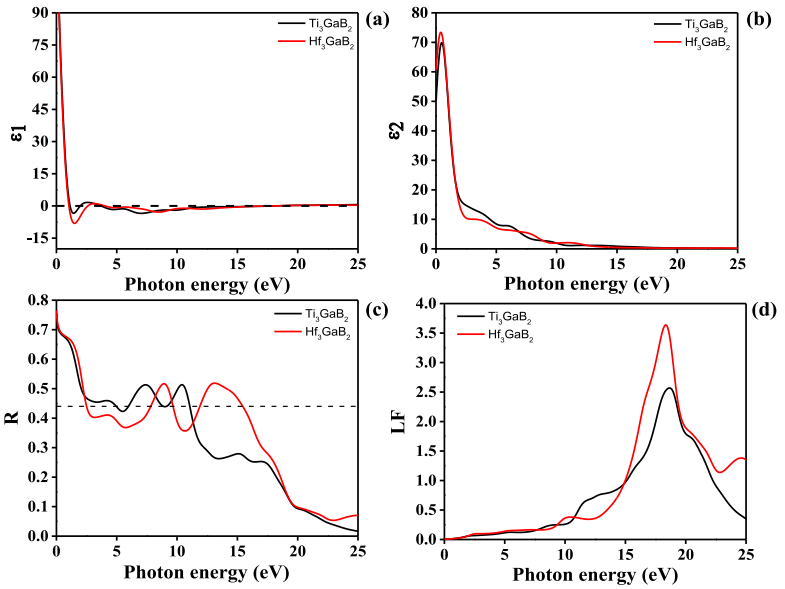

Fig. 4. (a) Real part of dielectric constant, ε_1 (b) Imaginary part of dielectric constant, ε_2 (c) Reflectivity, R and (d) Loss function, LF of Ti_3GaB_2 and Hf_3GaB_2 for [100] electric field directions.

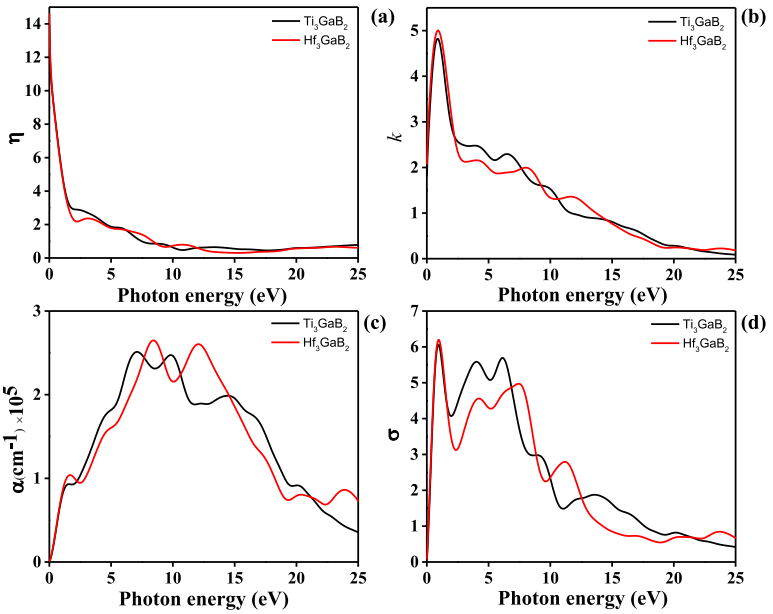

Fig. 5. The graphical representation of optical properties (a) refractive index (*n*), (b) extinction coefficient (*k*), (c) absorption coefficient (α), (d) Photoconductivity (σ).

excitation, and the corresponding frequency is referred to as the material's plasma frequency (ω_p). The plasma frequency for Ti_3GaB_2 and Hf_3GaB_2 is noted at 18.67 eV and 18.37 eV, respectively. This is consistent with the results for Zr_3PbC_2, which has a plasma frequency of 17.72 eV and exhibits a similar curve pattern. The refractive index of a material, expressed as N(ω) = n(ω) + ik(ω), is a significant characteristic. The real component, n(ω), calculated by Eq. (10):

$$n(\omega) = \frac{1}{\sqrt{2}}\left[\sqrt{\{\varepsilon_1(\omega)\}^2 + \{\varepsilon_2(\omega)\}^2} + \varepsilon_1(\omega)\right]^{1/2} \tag{10}$$

which influences the phase velocity, while the extinction coefficient, k(ω), determines the level of absorption loss experienced by an electromagnetic wave while traversing the material. Fig. 5(a) shows that the refractive index is high at low energy levels and declines as energy increases. The static refractive index value, n(0), for Ti_3GaB_2, is 13.93, and for Hf_3GaB_2, it is 14.64. Fig. 5(b) illustrates the extinction coefficient, where the peak for k(ω) is observed at approximately 0.8 eV for both Ti_3HfB_2 and Hf_3GaB_2, with values of 4.82 and 4.99, respectively. In both materials, the refractive index curve initiates a decrease as photon energy increases. The variation of the *n* and *k* spectra with photon energy shows good agreement with those of Zr_3PbC_2, as calculated by M.R. Rana et al.[64]. The static value is n(0)≈10, which is lower than that of Ti_3GaB_2 and Hf_3GaB_2.

Fig. 5(c) presents the absorption coefficient of M_3GaB_2 (M = Ti, Hf) calculated by Eq. (11):

$$\alpha(\omega) = \sqrt{2}\omega\left[\sqrt{\{\varepsilon_1(\omega)\}^2 + \{\varepsilon_2(\omega)\}^2} - \varepsilon_1(\omega)\right]^{1/2} \tag{11}$$

Owing to the absence of a band gap, the spectra of M_3GaB_2 (M = Ti, Hf) compounds commence at zero photon energy, indicating their metallic characteristics. The highest peak for Ti_3GaB_2 in the absorption coefficient occurs at 7.11 eV with a magnitude of 2.51 × 10^5 cm^{-1}. For Hf_3GaB_2, the maximum peak is at 8.42 eV with a magnitude of 2.65 × 10^5 cm^{-1}. Fig. 5(d) illustrates the photoconductivity of Hf_3GaB_2 described by, $\sigma(\omega) = \frac{\omega\varepsilon_2}{4\pi}$ representing the augmentation in electric conductivity following photon absorption. The photoconductivity peaks at the infrared (IR) region for both compounds, occurring at approximately 6.20 eV. In the ultraviolet (UV) region, there are notable peaks with a gradual decline in conductivity as photon energy increases for both materials.

4. Conclusion

In this study, we provide a comprehensive understanding of the physical, mechanical, and electronic properties of M_3GaB_2 (M = Ti, Hf) compounds through density functional theory calculations. Our investigation affirms the structural resemblance of these compounds to MAX phases, as evidenced by their negative formation energies, indicating stability. Analysis of the electronic band structure and density of states (DOS) revealed their metallic nature, with evident hybridization among different electronic states in the partial DOS. Fermi surface calculations corroborated these findings, further validating their metallic character. Determination of elastic

constants confirmed mechanical stability, with Ti_3GaB_2 displaying brittleness and Hf_3GaB_2 exhibiting ductility. Additionally, calculated elastic moduli and Vickers hardness measurements highlighted their soft nature, similar to other MAX phases, suggesting high malleability. The examination of optical properties affirmed the metallic nature of the M_3GaB_2 compound and highlighted Ti_3GaB_2 as a viable candidate for solar heating mitigation coatings, with Hf_3GaB_2 demonstrating comparable potential. This study is the first report on the 312 MAX phase borides, thus, the findings of this study will provide valuable guidance in predicting more MAX phases boride compounds [M_3AB_2] and can help advance the development of materials with desirable characteristics.

Data availability statement

The article contains all the data necessary to support the study's conclusions. On request, readers may obtain more information about this paper from the corresponding authors.

CRediT authorship contribution statement

A.K.M. Naim Ishtiaq: Writing – review & editing, Writing – original draft, Methodology, Investigation, Formal analysis. **Md Nasir Uddin:** Writing – review & editing, Writing – original draft, Methodology, Investigation, Formal analysis. **Noor Afsary:** Writing – review & editing, Writing – original draft, Investigation, Formal analysis. **Md Koushik Alam:** Writing – review & editing, Writing – original draft. **Shariful Islam:** Writing – review & editing. **Md Omar Faruk Rasel:** Writing – review & editing. **Md Ashraf Ali:** Writing – review & editing, Supervision. **Karimul Hoque:** Writing – review & editing, Supervision.

Declaration of competing interest

The authors declare that they have no known competing financial interests or personal relationships that could have appeared to influence the work reported in this paper.

References

[1] M. Sokol, V. Natu, S. Kota, M.W. Barsoum, On the chemical diversity of the MAX phases, in: Trends in Chemistry, vol. 1, Elsevier BV, May 2019, pp. 210–223, https://doi.org/10.1016/j.trechm.2019.02.016, 2.

[2] J. Zhou, M. Dahlqvist, J. Björk, J. Rosen, Atomic scale design of MXenes and their parent Materials—From theoretical and experimental perspectives, Chem. Rev. 123 (23) (Nov. 2023) 13291–13322, https://doi.org/10.1021/acs.chemrev.3c00241.

[3] L. Fu, W. Xia, "MAX phases as nanolaminate materials: chemical composition, microstructure, synthesis, properties, and applications,", Adv. Eng. Mater. 23 (4) (Jan. 2021) 2001191 https://doi.org/10.1002/adem.202001191.

[4] Md Nasir Uddin, A.K.M. Naim Ishtiaq, S. Islam, Md Rasel Rana, Md Ashraf Ali, K. Hoque, Prediction of new 212 M2AB2 borides as a promising candidate for future engineering: DFT calculations, Mater. Today Commun. 39 (Jun. 2024), https://doi.org/10.1016/j.mtcomm.2024.108536, 108536–108536.

[5] R. Samia, et al., Electronic, elastic and piezoelectric properties calculations of perovskites materials type BiXO3(X = Al, Sc): DFT and DFPT investigations, Chem. Phys. 573 (Sep. 2023), https://doi.org/10.1016/j.chemphys.2023.111998, 111998–111998.

[6] M. Dahlqvist, M.W. Barsoum, J. Rosén, MAX phases – past, present, and future, Mater. Today (Dec. 2023), https://doi.org/10.1016/j.mattod.2023.11.010.

[7] Z. Zhang, X. Duan, D. Jia, Y. Zhou, S. van der Zwaag, On the formation mechanisms and properties of MAX phases: a review, J. Eur. Ceram. Soc. 41 (7) (Jul. 2021) 3851–3878, https://doi.org/10.1016/j.jeurceramsoc.2021.02.002. Elsevier BV.

[8] J. Gonzalez-Julian, Processing of MAX phases: from synthesis to applications, J. Am. Ceram. Soc. 104 (2) (Nov. 15, 2020) 659–690, https://doi.org/10.1111/jace.17544. Wiley.

[9] N. Kubitza, C. Büchner, J. Sinclair, R.M. Snyder, C.S. Birkel, Extending the chemistry of layered solids and nanosheets: chemistry and structure of MAX phases, MAB phases and MXenes, ChemPlusChem 88 (8) (Aug. 2023), https://doi.org/10.1002/cplu.202300214. Wiley.

[10] P. Eklund, J. Rosen, P. Persson, Layered ternary $M_{n+1}AX_n$ phases and their 2D derivative MXene: an overview from a thin-film perspective, J. Phys. D 50 (11) (Feb. 2017), https://doi.org/10.1088/1361-6463/aa57bc, 113001–113001.

[11] Gokhan Surucu, Hasan Huseyin Gullu, Abdullah Candan, B. Yildiz, Aytac Erkisi, First-principles studies of Tin+1SiNn (n = 1, 2, 3) MAX phase, The Philosophical Magazine A Journal of Theoretical Experimental and Applied Physics 100 (17) (May 2020) 2183–2204, https://doi.org/10.1080/14786435.2020.1759835.

[12] M.A. Pietzka, J.C. Schuster, Summary of constitutional data on the Aluminum-Carbon-Titanium system, in: Journal of Phase Equilibria, vol 15, Springer Science and Business Media LLC, Aug. 1994, pp. 392–400, https://doi.org/10.1007/bf02647559, 4.

[13] Z. Lin, M. Zhuo, Y. Zhou, M. Li, J. Wang, Microstructures and theoretical bulk modulus of layered ternary tantalum aluminum carbides, J. Am. Ceram. Soc. 89 (12) (Nov. 10, 2006) 3765–3769, https://doi.org/10.1111/j.1551-2916.2006.01303.x. Wiley.

[14] T. Lapauw, et al., Synthesis of MAX phases in the Hf–Al–C system, Am. Chem. Soc. 55 (21) (Oct. 11, 2016) 10922–10927, https://doi.org/10.1021/acs.inorgchem.6b01398. Inorganic Chemistry.

[15] T. Lapauw, et al., Synthesis of the novel Zr 3 AlC 2 MAX phase, J. Eur. Ceram. Soc. 36 (3) (Feb. 2016) 943–947, https://doi.org/10.1016/j.jeurceramsoc.2015.10.011. Elsevier BV.

[16] T. Lapauw, B. Tunca, T. Cabioc'h, J. Vleugels, K. Lambrinou, Reactive spark plasma sintering of Ti3SnC2, Zr3SnC2 and Hf3SnC2 using Fe, Co or Ni additives, J. Eur. Ceram. Soc. 37 (15) (Dec. 2017) 4539–4545, https://doi.org/10.1016/j.jeurceramsoc.2017.06.041. Elsevier BV.

[17] M. Li, et al., Element replacement approach by reaction with lewis acidic molten salts to synthesize nanolaminated MAX phases and MXenes, J. Am. Chem. Soc. 141 (11) (Mar. 01, 2019) 4730–4737, https://doi.org/10.1021/jacs.9b00574. American Chemical Society (ACS).

[18] Q. Zhang, et al., Synthesis of new lead-containing MAX phases of Zr3PbC2 and Hf3PbC2, J. Am. Ceram. Soc. 106 (11) (Jul. 21, 2023) 6390–6397, https://doi.org/10.1111/jace.19332. Wiley.

[19] M. Khazaei, M. Arai, T. Sasaki, M. Estili, Y. Sakka, Trends in electronic structures and structural properties of MAX phases: a first-principles study on M2AlC (M = Sc, Ti, Cr, Zr, Nb, Mo, Hf, or Ta), M2AlN, and hypothetical M2AlB phases, J. Phys. Condens. Matter 26 (50) (Nov. 24, 2014) 505503, https://doi.org/10.1088/0953-8984/26/50/505503. IOP Publishing.

[20] G. Surucu, Investigation of structural, electronic, anisotropic elastic, and lattice dynamical properties of MAX phases borides: an Ab-initio study on hypothetical MAB (M = Ti, Zr, Hf; A = Al, Ga, In) compounds, Mater. Chem. Phys. 203 (Jan. 2018) 106–117, https://doi.org/10.1016/j.matchemphys.2017.09.050. Elsevier BV.

[21] N. Miao, et al., Computational prediction of boron-based MAX phases and MXene derivatives, Am. Chem. Soc. 32 (16) (Jul. 22, 2020) 6947–6957, https://doi.org/10.1021/acs.chemmater.0c02139. Chemistry of Materials.

[22] M.A. Ali, M.M. Hossain, M.M. Uddin, M.A. Hossain, A.K.M.A. Islam, S.H. Naqib, Physical properties of new MAX phase borides M2SB (M = Zr, Hf and Nb) in comparison with conventional MAX phase carbides M2SC (M = Zr, Hf and Nb): comprehensive insights, J. Mater. Res. Technol. 11 (Mar. 2021) 1000–1018, https://doi.org/10.1016/j.jmrt.2021.01.068. Elsevier BV.

[23] T. Rackl, D. Johrendt, The MAX phase borides Zr2SB and Hf2SB, Solid State Sci. 106 (Aug. 2020) 106316, https://doi.org/10.1016/j.solidstatesciences.2020.106316. Elsevier BV.

[24] S. Sâad Essaoud, A.S. Jbara, Electronic-structural, thermo-electric, and thermo-mechanical properties of M2AC and M2AB (M = Nb or Mo, A = Al or Ga) compounds, Indian J. Phys. 97 (1) (Jun. 08, 2022) 105–114, https://doi.org/10.1007/s12648-022-02386-0. Springer Science and Business Media LLC.

[25] M.R. Rana, et al., DFT prediction of the stability and physical properties of M2GaB (M = Sc, V, Nb, Ta), J. Mater. Res. Technol. 24 (May 2023) 7795–7815, https://doi.org/10.1016/j.jmrt.2023.05.008. Elsevier BV.

[26] S. Islam, et al., A comprehensive exploration of the physical properties of M2GaB (M = Ti, Zr, Mo, Hf) through DFT method, Results Mater. 19 (Sep. 2023) 100438, https://doi.org/10.1016/j.rinma.2023.100438. Elsevier BV.

[27] S.J. Clark, et al., First principles methods using CASTEP, Z. für Kristallogr. - Cryst. Mater. 220 (5/6) (Jan. 2005), https://doi.org/10.1524/zkri.220.5.567.65075.

[28] M.D. Segall, et al., First-principles simulation: ideas, illustrations and the CASTEP code, J. Phys. Condens. Matter 14 (11) (Mar. 2002) 2717–2744, https://doi.org/10.1088/0953-8984/14/11/301.

[29] J.P. Perdew, K. Burke, M. Ernzerhof, Generalized gradient approximation made simple, Phys. Rev. Lett. 77 (18) (Oct. 1996) 3865–3868, https://doi.org/10.1103/physrevlett.77.3865.

[30] Y. Wang, P. Wisesa, A. Balasubramanian, S. Dwaraknath, T. Mueller, Rapid generation of optimal generalized Monkhorst-Pack grids, Comput. Mater. Sci. 187 (Feb. 2021) 110100, https://doi.org/10.1016/j.commatsci.2020.110100.

[31] T.H. Fischer, J. Almlof, General methods for geometry and wave function optimization, J. Phys. Chem. 96 (24) (Nov. 1992) 9768–9774, https://doi.org/10.1021/j100203a036. American Chemical Society (ACS).

[32] D.T. Cuskelly, E.R. Richards, E.H. Kisi, V.J. Keast, Ti3GaC2 and Ti3InC2: First bulk synthesis, DFT stability calculations and structural systematics, in: Journal of Solid State Chemistry 230, Elsevier BV, Oct. 2015, pp. 418–425, https://doi.org/10.1016/j.jssc.2015.07.028.

[33] M. Roknuzzaman, et al., First hafnium-based MAX phase in the 312 family, Hf3AlC2: A first-principles study, in: Journal of Alloys and Compounds 727, Elsevier BV, Dec. 2017, pp. 616–626, https://doi.org/10.1016/j.jallcom.2017.08.151.

[34] M.W. Qureshi, X. Ma, G. Tang and, R. Paudel, "Ab initio predictions of structure and physical properties of the Zr2GaC and Hf2GaC MAX phases under pressure,", in: Scientific Reports 11, Springer Science and Business Media LLC, Feb. 05, 2021 no. 1.

[35] J. Islam, et al., DFT insights into MAX phase borides Hf2AB [A = S, Se, Te] in comparison with MAX phase carbides Hf2AC [A = S, Se, Te], ACS Omega 8 (36) (Aug. 2023) 32917–32930, https://doi.org/10.1021/acsomega.3c04283.

[36] L. Samia, et al., Investigation of structural, elastic, electronic, and magnetic proprieties for X2LuSb (X = Mn and Ir) full-Heusler alloys, Emergent materials 5 (2) (Feb. 2022) 537–551, https://doi.org/10.1007/s42247-022-00374-y.

[37] M.W. Barsoum, "MAX Phases.", Wiley, Aug. 09, 2013 https://doi.org/10.1002/9783527654581.

[38] C.Q. Sun, Dominance of broken bonds and non-bonding electrons at the nanoscale, in: Nanoscale 2, Royal Society of Chemistry (RSC, 2010, p. 1930, https://doi.org/10.1039/c0nr00245c.

[39] L. Drici, et al., First-principles calculations of structural, elastic, electronic, and optical properties of CaYP (Y = Cu, Ag) Heusler alloys, Emergent Materials, Mar (2021). https://doi.org/10.1007/s42247-021-00211-8.

[40] E. Güler, M. Güler, G. Uğur, A first-principles study for the elastic and mechanical properties of Ti64, Ti6242 and Ti6246 alloys, Eur. Phys. J. B (2021). https://doi.org/10.1140/epjb/s10051-021-00230-8.

[41] X. Liu, et al., First-principles calculations of mechanical and thermodynamic properties of tetragonal Be12Ti, RSC Advances 9 (10) (2019) 5302–5312. https://doi.org/10.1039/c8ra08711c.

[42] H. Chung, W.R. Buessem, "The Voigt-Reuss-Hill Approximation and Elastic Moduli of Polycrystalline MgO, CaF2, β-ZnS, ZnSe, and CdTe,", Journal of applied physics 38 (6) (May 1967) 2535–2540, https://doi.org/10.1063/1.1709944.

[43] D. Connétable, O. Thomas, First-principles study of the structural, electronic, vibrational, and elastic properties of orthorhombic NiSi, Physical Review B 79 (9) (Mar. 2009). https://doi.org/10.1103/physrevb.79.094101.

[44] M.A. Hadi, S.-R.G. Christopoulos, S.H. Naqib, A. Chroneos, M.E. Fitzpatrick, A. Islam, "Physical properties and defect processes of M3SnC2 (M = Ti, Zr, Hf) MAX phases: Effect of M-elements,", Journal of Alloys and Compounds 748 (Jun. 2018) 804–813, https://doi.org/10.1016/j.jallcom.2018.03.182.

[45] W. Tan, et al., Structural stability and physical properties of MAX phases M2SX (M=Sc, Y, X=B, C, N) via first-principles calculations, Physica scripta 98 (8) (Jul. 2023) 085938, 085938, https://doi.org/10.1088/1402-4896/ace500.

[46] A.A. Belkacem, et al., "The stability analysis and efficiency of the new MAX-phase compounds M3GaC2 (M: Ti or Zr): A first-principles assessment,", Results in Physics 38 (Jul. 2022) 105621, https://doi.org/10.1016/j.rinp.2022.105621.

[47] S.-R.G. Christopoulos, P.P. Filippatos, M.A. Hadi, N. Kelaidis, M.E. Fitzpatrick, A. Chroneos, "Intrinsic defect processes and elastic properties of Ti3AC2 (A = Al, Si, Ga, Ge, In, Sn) MAX phases,", in: Journal of Applied Physics, AIP Publishing, Jan. 09, 2018 https://doi.org/10.1063/1.5011374.

[48] M.A. Ali, M.W. Qureshi, Newly synthesized MAX phase Zr2SeC: DFT insights into physical properties towards possible applications, in: RSC Advances 11, Royal Society of Chemistry (RSC, 2021, pp. 16892–16905, https://doi.org/10.1039/d1ra02345d.

[49] O.N. Senkov, D.B. Miracle, "Generalization of intrinsic ductile-to-brittle criteria by Pugh and Pettifor for materials with a cubic crystal structure,", Scientific Reports 11 (1) (Feb. 2021) https://doi.org/10.1038/s41598-021-83953-z.

[50] S Lathifa Banu, Vasu Veerapandy, Helmer Fjellvåg, Ponniah Vajeeston, "First-Principles Insights into the Relative Stability, Physical Properties, and Chemical Properties of MoSe2,", ACS Omega 8 (15) (Apr. 2023) 13799–13812, https://doi.org/10.1021/acsomega.2c08217.

[51] M.A. Hadi, et al., A density functional theory approach to the effects of C and N substitution at the B-site of the first boride MAX phase Nb2SB, in: Materials Today Communications 29, Elsevier BV, Dec. 2021, p. 102910, https://doi.org/10.1016/j.mtcomm.2021.102910.

[52] X.Q. Chen, H. Niu, D. Li, Y. Li, Modeling hardness of polycrystalline materials and bulk metallic glasses, Intermetallics 19 (9) (2011) 1275–1281, https://doi.org/10.1016/j.intermet.2011.03.026.

[53] Ali Md Ashraf, Hossain Md Mukter, Uddin Md Mohi, A. Islam, Naqib Saleh Hasan, The rise of 212 MAX phase borides: DFT insights into the physical properties of Ti2PB2, Zr2PbB2, and Nb2AB2 [A = P, S] for thermomechanical applications, ACS Omega 8 (1) (Dec. 2022) 954–968, https://doi.org/10.1021/acsomega.2c06331.

[54] F. Gao, "Theoretical model of intrinsic hardness,", in: Physical Review B 73, American Physical Society (APS), Apr. 26, 2006 https://doi.org/10.1103/physrevb.73.132104 no. 13.

[55] M. Wang, Y. Li, T. Cui, Y. Ma, G. Zou, "Origin of hardness in WB4 and its implications for ReB4, TaB4, MoB4, TcB4, and OsB4,", in: Applied Physics Letters 93, AIP Publishing, Sep. 08, 2008 https://doi.org/10.1063/1.2977760 no. 10.

[56] M.T. Nasir, et al., First-principles study of superconducting ScRhP and ScIrP pnictides, Phys. Status Solidi 254 (11) (Aug. 2017) 1700336, https://doi.org/10.1002/pssb.201700336.

[57] F.-Z. Dai, Y. Zhou, "A Modified Theoretical Model of Intrinsic Hardness of Crystalline Solids,", Scientific Reports 6 (1) (Sep. 2016) https://doi.org/10.1038/srep33085.

[58] M.W. Barsoum, M. Radovic, "Elastic and Mechanical Properties of the MAX Phases,", Annual Review of Materials Research 41 (1) (Aug. 04, 2011) https://doi.org/10.1146/annurev-matsci-062910-100448.

[59] S. Li, R. Ahuja, M.W. Barsoum, P. Jena, B. Johansson, "Optical properties of Ti3SiC2 and Ti4AlN3,", in: Applied Physics Letters 92, AIP Publishing, Jun. 02, 2008 https://doi.org/10.1063/1.2938862 no. 22.

[60] Anwar ul Haq, et al., A first principle investigation of electronic, mechanical, optical and transport properties of A2AgAlI6(A = Rb, K, Na) for energy harvesting, Physica scripta 98 (11) (Oct. 2023) 115972, 115972, https://doi.org/10.1088/1402-4896/ad032c.

[61] X. Li, H.-L. Cui, R.-Z. Zhang, First-principles study of the electronic and optical properties of a new metallic MoAlB 6 (1) (Dec. 2016). https://doi.org/10.1038/srep39790.
[62] S. Al-Qaisi, et al., First-principles calculations to investigate electronic, structural, optical, and thermoelectric properties of semiconducting double perovskite Ba2YBiO6, in: Micro and Nanostructures 170, Elsevier BV, Oct. 2022, p. 207397, https://doi.org/10.1016/j.micrna.2022.207397.
[63] S. Al-Qaisi, et al., First-principles investigations of Na2CuMCl6 (M = Bi, Sb) double perovskite semiconductors: Materials for green technology, in: Materials Science in Semiconductor Processing 150, Elsevier BV, Nov. 2022, p. 106947, https://doi.org/10.1016/j.mssp.2022.106947.
[64] M.R. Rana, S. Islam, K. Hoque, S. Mahmud, M.A. Ali, Newly synthesized Pb-based 312 MAX phases M3PbC2 (M = Zr and Hf): A First-principles study, in: Diamond and Related Materials 146, Elsevier BV, Jun. 2024, p. 111245, https://doi.org/10.1016/j.diamond.2024.111245.